

# Electroactive soft actuators utilizing PEDOT:PSS and 3D lithium-ion-conducting phosphate columnar liquid crystals embedded in a porous polyethylene membrane

Chengyang Liu<sup>a,b</sup> and Masafumi Yoshio<sup>a,b,c,d</sup>

<sup>a</sup>Research Center for Macromolecules and Biomaterials, National Institute for Materials Science, Tsukuba, Ibaraki, Japan;

<sup>b</sup>Graduate School of Chemical Sciences and Engineering, Hokkaido University, Sapporo, Hokkaido, Japan;

<sup>c</sup>Research Center for Autonomous Systems Materialogy (ASMat), Institute of Integrated Research, Institute of Science Tokyo, Yokohama, Kanagawa, Japan;

<sup>d</sup>Japan Science and Technology Agency, Precursory Research for Embryonic Science and Technology (PRESTO), Kawaguchi, Saitama, Japan

## ABSTRACT

This study introduces a novel supramolecular thermotropic columnar liquid-crystalline (LC) electrolyte tailored for high-performance ionic electroactive polymer (iEAP) actuators. The electrolyte is designed by integrating lithium salts into a taper-shaped molecule with bisphosphate moieties (BPO), which self-assembles into a columnar hexagonal (Col<sub>h</sub>) phase, forming 3D continuous ion-conductive pathways. This architecture achieves high ionic conductivity of up to  $2 \times 10^{-4} \text{ S cm}^{-1}$  at room temperature. An actuator was fabricated by embedding this electrolyte into a microporous polyethylene membrane, sandwiched between PEDOT:PSS electrodes. The resulting device exhibits exceptional performance, achieving a bending strain of 0.52% and a force output of 0.5 mN under a  $\pm 2 \text{ V}$ , along with outstanding durability, retaining its performance over 9000 cycles. These results underscore the potential of 3D ion-conductive LC electrolytes in advancing iEAP actuator technologies, paving the way for innovative applications in tactile interfaces and soft robotics.

## ARTICLE HISTORY

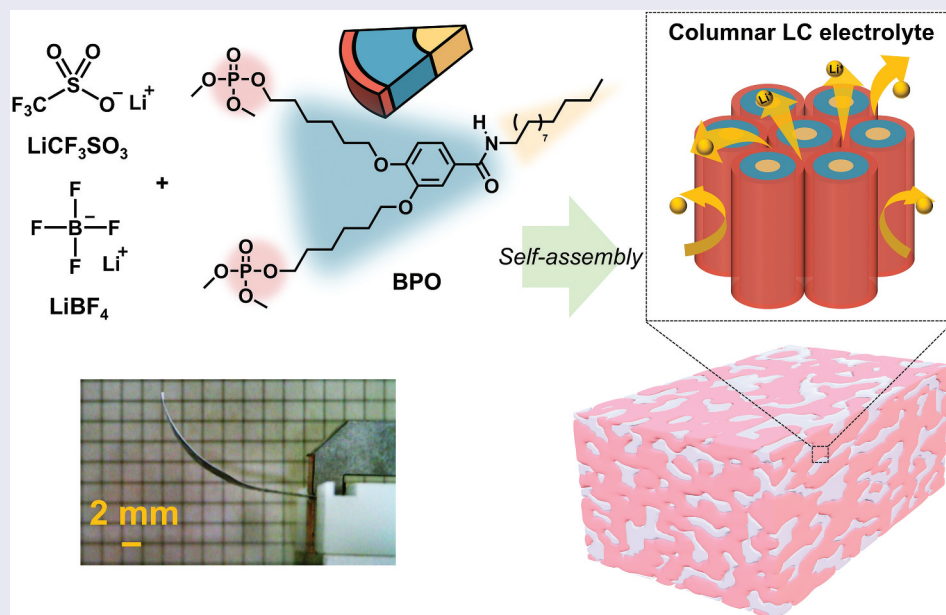
Received 27 December 2024

Revised 13 February 2025

Accepted 2 March 2025

## KEYWORDS


Ionic liquid crystal; actuator; composite electrolyte; columnar phase; ion pathway



## IMPACT STATEMENT

This study introduces a 3D ion-conductive liquid-crystalline electrolyte embedded in a porous polyethylene membrane with high ionic conductivity and durability, enabling high-performance iEAP actuators for practical application.

**CONTACT** Masafumi Yoshio  [YOSHIO.Masafumi@nims.go.jp](mailto:YOSHIO.Masafumi@nims.go.jp)  Research Center for Macromolecules and Biomaterials, National Institute for Materials Science, 1-2-1 Sengen, Tsukuba, Ibaraki 305-0047, Japan

 Supplemental data for this article can be accessed online at <https://doi.org/10.1080/14686996.2025.2475738>

© 2025 The Author(s). Published by National Institute for Materials Science in partnership with Taylor & Francis Group.

This is an Open Access article distributed under the terms of the Creative Commons Attribution-NonCommercial License (<http://creativecommons.org/licenses/by-nc/4.0/>), which permits unrestricted non-commercial use, distribution, and reproduction in any medium, provided the original work is properly cited. The terms on which this article has been published allow the posting of the Accepted Manuscript in a repository by the author(s) or with their consent.

## 1. Introduction

Amphiphilic liquid-crystalline (LC) compounds, composed of ionophobic and ionophilic blocked structures, represent a promising platform for non-volatile organic electrolyte materials due to their ability to form long-range ordered and orientable ion-transport pathways [1–7]. To date, a variety of LC molecules exhibiting 1D columnar, 2D layered, and 3D micellar cubic and bicontinuous cubic structures have been explored as electrolytes in electrochemical devices, including lithium-ion batteries, dye-sensitized solar cells, fuel cells, and electrochromic displays [8–12]. For instance, cyclic carbonate-terminated rod-shaped mesogenic compounds, in combination with liquid propylene carbonate, have been engineered to create 2D lithium-ion transport pathways and successfully applied to lithium-ion batteries [13]. Additionally, layered, columnar, and bicontinuous cubic LC structures have been designed using calamitic and dendritic mesogenic molecules functionalized with poly(ethylene oxide)s and crown ethers [1,6,14–16]. Furthermore, ionic liquid-derived LC electrolytes and zwitterionic LC materials have been developed as proton conductors in the presence of water [11,17]. Despite these advancements, designing solvent-free LC electrolytes with both high lithium-ion solubility and ionic conductivities exceeding  $10^{-4}$  S cm<sup>-1</sup> at room temperature remains a significant challenge.

LC electrolytes also offer exciting potential for innovative applications, such as the development of low-voltage-driven ionic electroactive polymer (iEAP) actuators [18–21] capable of converting electrical energy into mechanical deformation. These actuators are particularly promising for bio-mimetic robots and medical devices. Recently, we have focused on developing iEAP actuators that harness the unique properties of photocured LC polymer electrolytes and low-molecular-weight LC polymer gel electrolytes [22,23]. These materials, incorporating mobile imidazolium and lithium cations, are sandwiched between flexible conductive polymer films made of poly(3,4-ethylenedioxythiophene) doped with poly(stylenesulfonic acid) (PEDOT:PSS). Despite their low ion contents, these actuators demonstrate rapid and large bending deformations and generate high blocking forces under low alternating current (AC) voltages ( $\leq 2$  V). This performance is driven by ion distribution imbalances within the electrolytes, the formation of electric double-layer capacitance at electrode/electrolyte interfaces, and electrode redox reactions. These soft actuators hold significant promise for advanced applications in soft robotics and haptic technologies [24,25].

To further enhance actuation performance, structural engineering of electrolytes is critical. A key challenge for LC electrolytes in iEAP actuators lies in

achieving efficient ion transport while maintaining sufficient mechanical strength, flexibility, and prevention of short circuits between electrodes. One potential approach involves increasing the ion content in the LC electrolyte. However, the incorporation of ionic liquids often softens the electrolyte, reducing its ability to generate strong forces. Similarly, the use of polyethers limits the solubility of lithium salts, leading to a significant decrease in conductivity as ion content increases [16,26]. Furthermore, photopolymerization of LC electrolytes and polymer blending to create self-supporting membranes typically reduce ion mobility [27,28]. As a result, 3D lithium-ion conductive LC electrolytes with integrated polymer frameworks – free from macroscopic orientation and strong intermolecular interactions between the polymer and LC electrolytes – emerge as an ideal solution.

In this study, we introduce a novel strategy for fabricating electrolyte membranes by embedding a 3D ion-transporting columnar LC electrolyte into a porous polyethylene matrix. The LC electrolyte is based on a room-temperature columnar liquid crystal composed of a taper-shaped molecule with bisphosphate groups (BPO), complexed with lithium salts (Figure 1(a)). This columnar structure features ionic shells surrounding lipophilic cores, formed through ion – dipolar complexation with lithium salts, enabling 3D ion transport. By embedding this LC electrolyte within a porous polymer network (Figure 1(b)) and incorporating conductive polymer electrodes, we achieved outstanding actuation performance, characterized by high bending strain, robust force generation under  $\pm 2$  V input, and excellent durability.

## 2. Experimental section

### 2.1. Materials

Ethyl 3,4-dihydroxybenzoate, dodecylamine, 4-(4,6-dimethoxy-1,3,5-triazin-2-yl)-4-methylmorpholinium chloride (DMTMM), dimethyl chlorophosphate, lithium tetrafluoroborate (LiBF<sub>4</sub>), dichloromethane, 4-dimethylaminopyridine (DMAP), and *N,N*-diisopropylethylamine (DIPEA) were purchased from Tokyo Chemical Industry (TCI, Japan). 6-Bromo-1-hexanol was purchased from Combi-Blocks. DMF, K<sub>2</sub>CO<sub>3</sub>, acetone, methanol, ethanol, and lithium triflate (LiCF<sub>3</sub>SO<sub>3</sub>) were purchased from Kanto Chemical (Cica, Japan). PEDOT:PSS (Clevios PH1000) was purchased from Heraeus.

### 2.2. General methods

<sup>1</sup>H and <sup>13</sup>C nuclear magnetic resonance (NMR) spectra were recorded on a JEOL ECZ 400S spectrometer. The chemical shifts ( $\delta$ ) are reported in ppm with the solvent peaks of CD<sub>2</sub>Cl<sub>2</sub> ( $\delta = 5.32$  ppm for <sup>1</sup>H NMR at 400

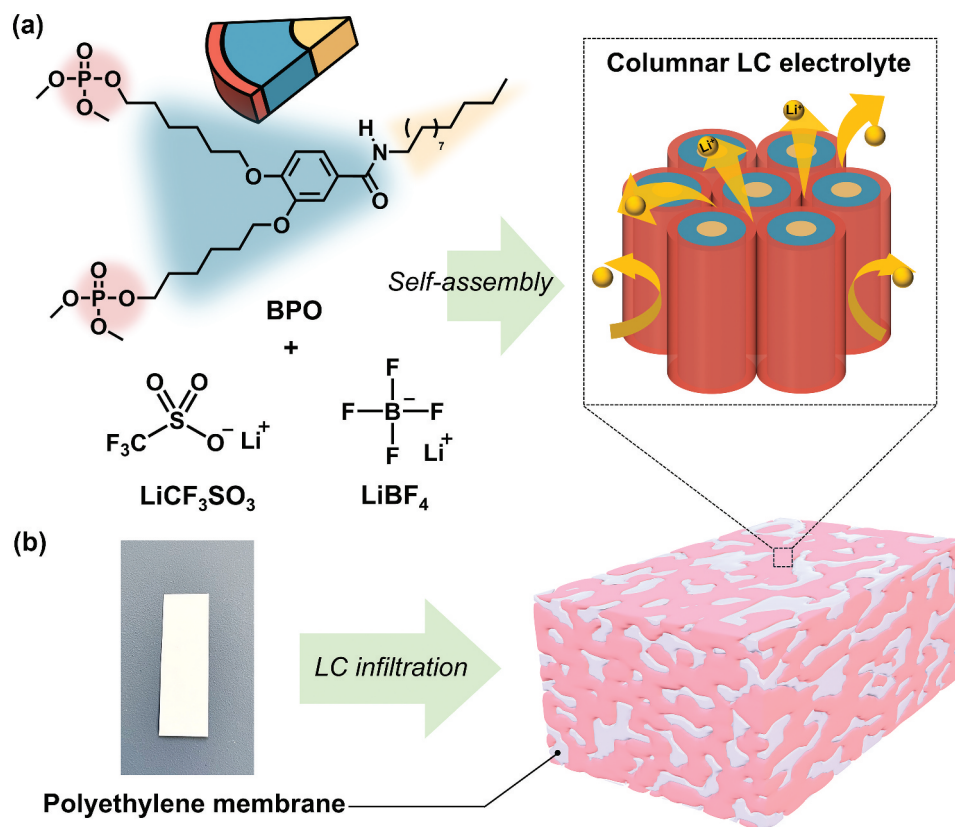


**Figure 1.** (a) Molecule structures of the taper-shaped dimethyl phosphate derivative (BPO) and lithium salts (LiCF<sub>3</sub>SO<sub>3</sub> and LiBF<sub>4</sub>) and illustration of the 3D continuous ion transport pathways formed in the nanosegregated columnar LC structure through the co-assembly of BPO, LiCF<sub>3</sub>SO<sub>3</sub>, and LiBF<sub>4</sub>. (b) Schematic representation of the infiltration of the 3D lithium-ion-conducting columnar liquid crystal into a porous polyethylene membrane, forming a self-standing, liquid crystal-filled polymer composite electrolyte membrane.

MHz) and CDCl<sub>3</sub> ( $\delta = 77.0$  ppm for <sup>13</sup>C NMR at 100 MHz) used as internal references. High-resolution mass spectrometry (HRMS) was performed on a Bruker micrOTOF II using positive atmospheric-pressure chemical ionization (APCI) as the ionization method. A polarized optical microscope (POM) (Olympus BX51N-31P-O3) equipped with a DP22 digital camera was employed to observe optical textures, with temperature control provided by a LINKAM T95-HS, LTS420E system. X-ray diffraction (XRD) patterns were recorded over a small angular range of  $2\theta = 1\text{--}30^\circ$  using a Rigaku MiniFlex 600 diffractometer with Ni-filtered Cu K $\alpha$  radiation. Fourier transform infrared (FT-IR) spectra were acquired with a Bruker ALPHA II spectrometer. Differential scanning calorimetry (DSC) measurements were carried out on a NETZSCH DSC-3500 Sirius system, with heating and cooling rates at  $10^\circ\text{C}/\text{min}$ .

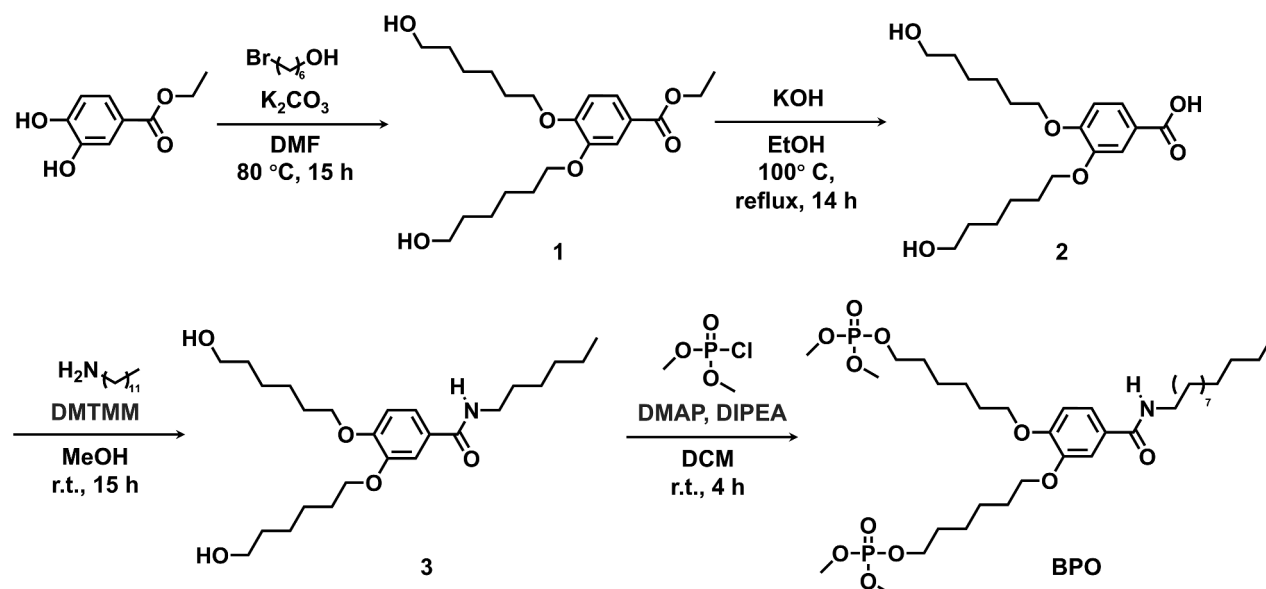
### 2.3. Synthesis of 1,2-Bis[6-(hexyl dimethyl phosphate)oxy]-4-dodecylcarbamoylbenzene (BPO)

The synthetic scheme of BPO is shown in Scheme 1.

**Synthesis of 1:** Ethyl 3,4-dihydroxybenzoate (1.51 g, 8.29 mmol), 6-bromo-1-hexanol (3.30 g, 18.2

mmol), and K<sub>2</sub>CO<sub>3</sub> (4.58 g, 33.2 mmol) were added to a flask. After replacing the air with argon, DMF was injected into the flask. The resulting mixture was stirred at  $80^\circ\text{C}$  for 15 h. The reaction mixture was then diluted with EtOAc and washed with a saturated NH<sub>4</sub>Cl aqueous solution. The organic phase was separated, dried over MgSO<sub>4</sub>, and filtered. After evaporating the solvent under reduced pressure, the residue was purified by silica gel column chromatography (CHCl<sub>3</sub>/EtOAc = 10/0 – 7/3) to give compound **1** as a colorless viscous liquid (yield: 97%). <sup>1</sup>H NMR (400 MHz, CDCl<sub>3</sub>)  $\delta = 7.64$  (dd,  $J = 8.5, 2.1$  Hz, ArH), 7.53 (d,  $J = 1.8$  Hz, ArH), 6.86 (d,  $J = 8.7$  Hz, ArH), 4.34 (q,  $J = 7.2$  Hz, 2 h; CH<sub>2</sub>), 4.05 (t,  $J = 6.4$  Hz, 4 h; CH<sub>2</sub>), 3.66 (t,  $J = 6.6$  Hz, 4 h; CH<sub>2</sub>), 1.89 – 1.81 (m, 4 h; CH<sub>2</sub>), 1.65 – 1.36 (m, 15 h; CH<sub>2</sub>, CH<sub>3</sub>). HRMS(APCI):  $m/z$  calcd. for C<sub>21</sub>H<sub>34</sub>O<sub>6</sub> [M]<sup>+</sup>, 382.2355; found, 382.2338.

**Synthesis of 2:** Compound **1** (2.80 g, 7.32 mmol) and KOH (2.05 g, 36.6 mmol) were dissolved in 30 mL of EtOH and 10 mL of water in a flask. The mixture was stirred and refluxed at  $100^\circ\text{C}$  for 14 h. Afterward, the reaction mixture was acidified with a 5% HCl aqueous solution, then diluted with EtOAc and deionized water. The organic phase was separated, dried over MgSO<sub>4</sub>, and the solvent was removed under reduced pressure to yield a residue. This residue was



**Scheme 1.** Synthetic scheme of BPO.

recrystallized from a mixture of *n*-hexene, EtOAc, and MeOH in a freezer. The resulting product, compound **2**, was obtained as a white solid (yield: 61%).  $^1\text{H}$  NMR (400 MHz,  $(\text{CD}_3)_2\text{CO}$ )  $\delta$  = 7.64 (dd,  $J$  = 8.5, 2.1 Hz, ArH), 7.54 (d,  $J$  = 1.8 Hz, ArH), 7.03 (q,  $J$  = 4.1 Hz, ArH), 4.12 – 4.03 (m, 4 h;  $\text{CH}_2$ ), 3.57 – 3.51 (m, 4 h;  $\text{CH}_2$ ), 1.89 – 1.78 (m, 4 h;  $\text{CH}_2$ ), 1.64 – 1.41 (m, 12 h;  $\text{CH}_2$ ). HRMS(APCI):  $m/z$  calcd. for  $\text{C}_{19}\text{H}_{30}\text{O}_6$  [ $\text{M} - \text{H}$ ] $^-$ , 353.1970; found, 353.1969.

**Synthesis of 3:** Compound **2** (1.00 g, 2.83 mmol) and dodecylamine (0.79 g, 4.24 mmol) were dissolved in 20 mL of MeOH in a flask. To this solution, 4-(4,6-dimethoxy-1,3,5-triazin-2-yl)-4-methylmorpholinium chloride (DMTMM) (1.17 g, 4.24 mmol) was added in one portion with stirring at room temperature under ambient air. The reaction mixture was stirred for 15 h at room temperature. Afterward, the solvent was removed under reduced pressure. The resulting residue was purified by silica gel column chromatography (EtOAc/MeOH = 10/0–8/2) and recrystallized from a mixture of EtOAc and *n*-hexane, yielding compound **3** (0.92 g, 1.76 mmol) as a white solid (yield: 62%).  $^1\text{H}$  NMR (400 MHz,  $\text{CDCl}_3$ ):  $\delta$  = 7.39 (d,  $J$  = 2.3 Hz, ArH), 7.21 (dd,  $J$  = 8.2, 2.3 Hz, ArH), 6.84 (d,  $J$  = 8.7 Hz, ArH), 6.10 (s, 1 h; NH), 4.07 – 4.01 (m, 4 h;  $\text{CH}_2$ ), 3.65 (t,  $J$  = 6.6 Hz, 4 h;  $\text{CH}_2$ ), 3.42 (t,  $J$  = 7.3 Hz, 2 h;  $\text{CH}_2$ ), 1.88 – 1.78 (m, 6 h;  $\text{CH}_2$ ), 1.64 – 1.25 (m, 30 h;  $\text{CH}_2$ ), 0.88 (t,  $J$  = 6.9 Hz, 3 h;  $\text{CH}_3$ ). HRMS(APCI):  $m/z$  calcd. for  $\text{C}_{31}\text{H}_{55}\text{NO}_5$  [ $\text{M} + \text{H}$ ] $^+$ , 522.4114; found, 522.4128.

**Synthesis of BPO:** Compound **3** (0.50 g, 0.97 mmol), 4-dimethylaminopyridine (0.47 g, 3.9 mmol), and *N,N*-diisopropylethylamine (1.25 g, 9.65 mmol) were dissolved in 20 mL of  $\text{CH}_2\text{Cl}_2$  in a flask. Dimethyl chlorophosphate (0.84 mL, 5.8 mmol) was

then added dropwise to the solution at room temperature. The reaction mixture was stirred for 4 h. The reaction was then quenched by adding MeOH, and the mixture was diluted with EtOAc. The resulting solution was sequentially washed with a saturated  $\text{NaHCO}_3$  aqueous solution, a 5% HCl aqueous solution, and brine. The organic phase was separated, dried over  $\text{MgSO}_4$ , and then filtered. After evaporating the solvent under reduced pressure, the residue was purified by silica gel column chromatography (EtOAc/MeOH = 100/0 – 95/5) to give compound BPO as a translucent white solid (yield: 81%).  $^1\text{H}$  NMR (400 MHz,  $\text{CD}_2\text{Cl}_2$ ):  $\delta$  = 7.38 (d,  $J$  = 2.3 Hz, 1 h; ArH), 7.28 (dd,  $J$  = 8.2, 1.8 Hz, 1 h; ArH), 6.90 (d,  $J$  = 8.2 Hz, 1 h; ArH), 6.24 (d,  $J$  = 5.5 Hz, 1 h; NH), 4.08 – 4.03 (m, 8 h;  $\text{CH}_2$ ), 3.75 (d,  $J$  = 11.0 Hz, 12 h;  $\text{CH}_3$ ), 3.40 (dd,  $J$  = 12.8, 7.3 Hz, 2 h;  $\text{CH}_2$ ), 1.89 – 1.45 (m, 18 h;  $\text{CH}_2$ ), 1.38 – 1.30 (m, 18 h;  $\text{CH}_2$ ), 0.91 (t,  $J$  = 6.9 Hz, 3 h;  $\text{CH}_3$ ).  $^{13}\text{C}$  NMR (100 MHz,  $\text{CDCl}_3$ )  $\delta$  = 167.2, 151.7, 148.8, 127.4, 119.6, 113.0, 112.4, 69.1, 68.9, 67.9, 67.8, 54.3, 54.3, 40.2, 32.0, 30.3, 30.2, 29.8, 29.7, 29.7, 29.6, 29.4, 29.4, 29.1, 29.0, 27.1, 25.6, 25.5, 25.2, 25.2, 22.7, 14.2. HRMS(APCI):  $m/z$  calcd. for  $\text{C}_{35}\text{H}_{65}\text{NO}_{11}\text{P}_2$  [ $\text{M} + \text{h}$ ] $^+$ , 738.4066; found, 738.4093.

## 2.4. Preparation of the liquid crystal complexes

BPO and lithium salts were combined in glass vials at molar ratios of 1:2, 1:2.5, 1:3, and 1:3.5, and then dissolved thoroughly in acetone. The lithium salts, referred to as LiTB, were composed of  $\text{LiCF}_3\text{SO}_3$  and  $\text{LiBF}_4$  in a 3:1 molar ratio. The vials containing these mixtures were placed in an oven and heated to 85°C to evaporate most of the solvent. The mixtures were



subsequently dried under reduced pressure for 8 hours for further use.

## 2.5. Preparation of the electrolyte membrane

A polyethylene microporous membrane (HIPORE™, Asahi Kasei Corporation, mean pore diameter: 150 nm, porosity: 40%) [29] with a thickness of 25  $\mu\text{m}$  was placed on a glass substrate and heated to 90°C. Next, 10 mg of BPO/LiTB(3.5) (with LiTB at 3.5 equivalents to BPO) was applied onto the porous membrane, coating it until the membrane changed from white to translucent. The glass substrate was then transferred to a vacuum oven and maintained at 90°C under reduced pressure for 30 minutes. Afterward, the infiltrated LC electrolyte membrane was carefully peeled off from the glass substrate for subsequent use.

## 2.6. Preparation of PEDOT:PSS electrode

A 3 ml solution of PEDOT:PSS and ethylene glycol (mixed in a 94:6 volume ratio) was applied to a 5 cm  $\times$  5 cm area on a glass substrate. The mixture was dried at 80°C, and then deionized water was added to detach the dried film. The jelly-like film was transferred onto a PTFE substrate and further dried at 110°C, resulting in a PEDOT:PSS electrode film with a thickness of 10  $\mu\text{m}$ .

## 2.7. Preparation of the actuator

The LC electrolyte-infiltrated porous membrane and PEDOT:PSS film were both cut to dimensions of 20 mm in length and 4 mm in width. The electrolyte membrane was sandwiched between two pieces of PEDOT:PSS film. The total thickness of the actuators was  $70 \pm 2 \mu\text{m}$ , accounting for the volume expansion that occurred in the polyolefin porous membrane (HIPORE™).

## 2.8. Electrochemical measurements

A comb-shaped gold electrode was employed to measure the electrochemical impedance spectroscopy (EIS) of the liquid crystal complexes, while a Swagelok-type cell with two stainless-steel electrodes was used to obtain the cyclic voltammetry (CV) curve of the actuator. The spacer thicknesses were 58  $\mu\text{m}$  for the comb-shaped gold electrode and 34  $\mu\text{m}$  for the Swagelok-type cell. All measurements were performed in an environment with a relative humidity of approximately 30–40%. The specific capacitance,  $C_s$  ( $\text{F cm}^{-2}$ ), was calculated using the equation:  $C_s = \frac{I \Delta V}{2 \nu S V}$ , where  $I$  (A) is the response current,  $\nu$  (V

$\text{s}^{-1}$ ) is the sweep rate of the voltage,  $S$  ( $\text{cm}^2$ ) is the electrode area, and  $V$  (V) is the voltage window.

## 2.9. Actuation performance tests

The actuator was clamped using copper foils placed between two stainless steel electrodes, which were connected to a potentiostat (Hokuto Denko, HAL3001A). AC square voltages, generated by a function generator (YOKOGAWA FG400 30 MHz), were controlled by the potentiostat. The bending performance of the actuator was measured using a laser displacement meter (Keyence, LK-HD500). Signals for voltage, current, and displacement were recorded using a digital logger (HIOKI LR8880). Actuation photographs were captured with a USB microscope camera (Sanwa Supply, 400-CAM058, Japan). The peak-to-peak strain ( $\epsilon$ ) in the frequency range of 1–80 Hz was calculated using the equation:  $\epsilon = 2\delta d \times 100/(\delta^2 + L^2)$ , where  $\delta$  is the peak-to-peak displacement (mm),  $d$  is the thickness of the actuator (mm), and  $L$  is the distance (mm) from the clamped end of the actuator to the laser irradiation point.

# 3. Results and discussion

## 3.1. Materials design

Organophosphates with flame-retardant properties have been employed in battery electrolyte applications, significantly enhancing device safety during operation [30–32]. Their moderate dielectric constant prevents excessively strong ionic interactions, while the electronegativity of the P=O group promotes cation dissociation from anions, enabling the efficient transport of cations between phosphate-containing molecules. Previous studies demonstrated that grafting a single phosphate group onto a rod-shaped mesogen could achieve promising levels of ionic conductivity. In this study, to further enhance ionic transport capabilities, we grafted two phosphate groups onto a fan-shaped molecule, resulting in the novel compound BPO. At room temperature, BPO forms a turbid, viscous solid without exhibiting an LC phase. However, when combined with specific salts, BPO can exhibit a hexagonal columnar ( $\text{Col}_h$ ) LC phase. Experiments with various ionic liquids and lithium salts of differing volumes and molecular weights demonstrated that the combination of  $\text{LiCF}_3\text{SO}_3$  and BPO produces a relatively stable columnar LC phases. However, their LC – isotropic liquid (Iso) transitions are near room temperature, which do not satisfy the requirements for an electrolyte in iEAP actuators. In contrast, the combination of  $\text{LiBF}_4$  and BPO yields a higher clearing point due to  $\text{LiBF}_4$ 's smaller anionic volume and its enhanced ability to interact with the phosphate moieties. Unfortunately,

$\text{LiBF}_4$  tends to crystallize out of the BPO mixture at room temperature. Therefore, it is hypothesized that partially replacing  $\text{LiCF}_3\text{SO}_3$  with  $\text{LiBF}_4$  in the mixture could elevate the LC – Iso transition temperature to meet the actuator's requirements. Ultimately, a molar ratio of 3:1 for  $\text{LiCF}_3\text{SO}_3$  to  $\text{LiBF}_4$  was established, and this blended salt was designated LiTB.

### 3.2. Liquid crystal properties

The mixture of compound BPO and LiTB is denoted as BPO/LiTB(x), where x represents the molar ratio of LiTB to BPO. A ratio of 3.5:1 was found to provide the highest ionic conductivity and mesophase stability without inducing unwanted crystallization. However, exceeding this threshold increases the susceptibility to crystallization. Fig. S1 shows the DSC curves of BPO/LiTB (3.5) during the first cooling and second heating scans, demonstrating that BPO/LiTB(3.5) maintains a stable LC phase at room temperature. Figure 2(a) illustrates the phase transition behaviour of the mixtures on heating as the lithium salts ratio varies, with C,  $\text{Col}_h$ , Iso representing the crystal phase, columnar hexagonal LC phase, and isotropic phase, respectively. As the lithium salt ratio increases, the transition temperature from C to  $\text{Col}_h$  shows a slight decrease. In contrast, the transition temperature from  $\text{Col}_h$  to Iso exhibits an upward trend between BPO/LiTB(2) and BPO/LiTB(3). However, the Iso –  $\text{Col}_h$  transition temperature of BPO/LiTB(3.5) is lower than that of BPO/LiTB(3), likely due to increased steric hindrance between molecules, which reduces intermolecular interaction forces.

To determine the structure of the  $\text{Col}_h$  LC phase, X-ray diffraction (XRD) analysis was conducted to examine the lattice parameters. In Figure 2(b), the XRD pattern of BPO/LiTB(3.5) reveals three distinct peaks at  $2\theta$  values of  $1.74^\circ$ ,  $3.04^\circ$ , and  $3.47^\circ$ . The reciprocal  $d$ -spacing ratio of the three peaks is  $1:\sqrt{3}:2$ , corresponding to the (100), (110), and (200) diffractions of the  $\text{Col}_h$

phase. The intercolumnar distance ( $a$ ) of BPO/LiTB(3.5) was calculated to be  $58 \text{ \AA}$  using the equation:  $a = 2\langle d \rangle / \sqrt{3}$ ,  $\langle d \rangle = (d_{100} + \sqrt{3}d_{110} + 2d_{200})/3$ . The number ( $n$ ) of molecules per disc in the hexagonal lattice was estimated to be approximately 5, based on the equation:  $n = \sqrt{3}N_A a^2 h \rho / 2M$ , where  $N_A$  is Avogadro's number ( $6.02 \times 10^{23} \text{ mol}^{-1}$ ),  $h$  is the average height of a stratum in a column ( $4.58 \text{ \AA}$ , determined from a halo peak at  $19.4^\circ$ ),  $M$  is the average molecular weight of BPO/LiTB(3.5) ( $M = 1612.00 \text{ g mol}^{-1}$ ), and the density ( $\rho$ ) was assumed to be  $1.0 \text{ g cm}^{-3}$ . Fig S2 depicts the relationship between lithium salt content and the intercolumnar distance. As the molar ratio of lithium salt increases, the intercolumnar distance increases. This phenomenon results from the effective participation of lithium salts in the self-assembly behaviour of BPO and the lithium salts, thereby facilitating the formation of ordered 3D ion pathways.

To gain insight into the interaction between BPO and LiTB, we utilized Fourier transform infrared (FT-IR) absorption spectra to observe changes in bond vibrations (Fig. S3). The stretching vibration peak of P=O bond in the BPO molecule shifts from  $1262$  to  $1256 \text{ cm}^{-1}$ , indicating that the lithium-ions can coordinate with the P=O moieties through ion – dipole interactions. Additionally, the amide N – H stretching and bending peaks of BPO, initially observed at  $3294$  and  $1542 \text{ cm}^{-1}$ , respectively, shift to  $3394$  and  $1558 \text{ cm}^{-1}$ . This shift is attributed to the dissociation of the intermolecular amide hydrogen bond ( $\text{C}=\text{O} \cdots \text{H} - \text{N}$ ) in the presence of LiTB, facilitated by anion coordination to the N – H groups, such as  $\text{N} - \text{H} \cdots \text{BF}_4^-$  anion and  $\text{N} - \text{H} \cdots \text{OSO}_2\text{CF}_3^-$  anion. These observations suggest that BPO possesses a strong capacity to dissociate lithium salts, thereby playing a pivotal role in enhancing the ionic conductivity.

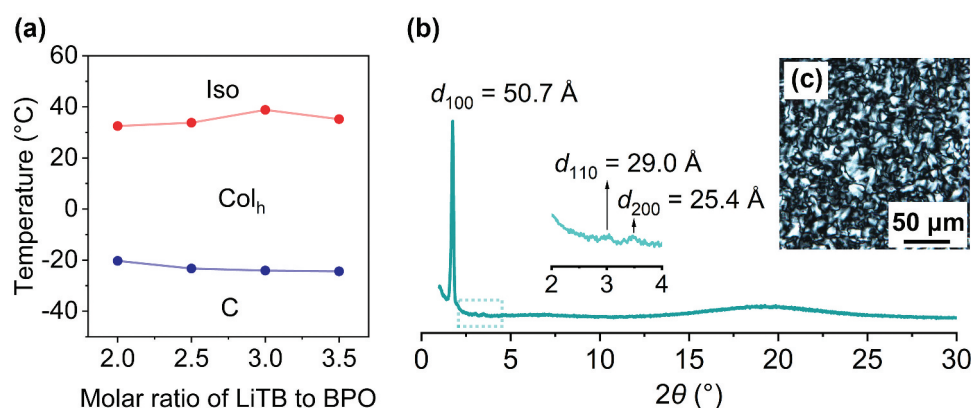


**Figure 2.** (a) Phase transition behaviour of the mixtures of BPO and lithium salts (LiTB,  $\text{LiCF}_3\text{SO}_3\text{:LiBF}_4 = 3:1$ ) on heating. (b) XRD pattern and (c) Polarized optical microscope image of BPO/LiTB(3.5) at room temperature.

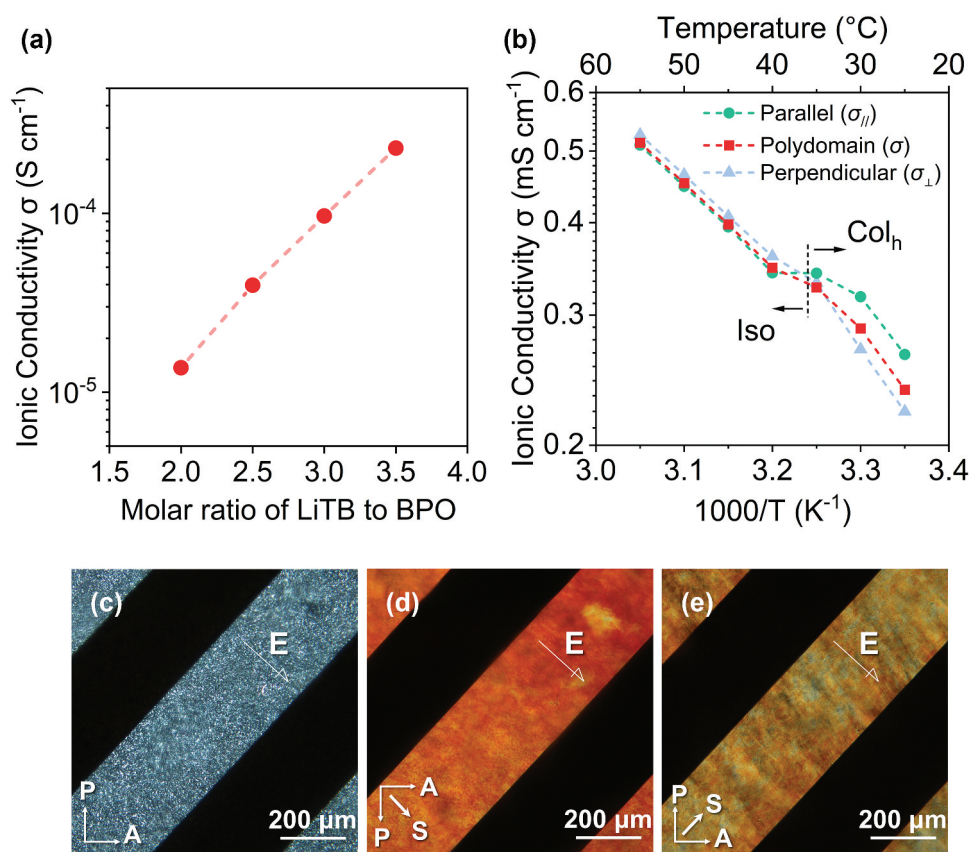


**Figure 3.** (a) Room temperature ionic conductivities of BPO/LiTB(*x*), where *x* = 2, 2.5, 3, 3.5. (b) Temperature-dependent ionic conductivities of BPO/LiTB(3.5) with planarly oriented columns on a glass substrate with comb-shaped gold electrodes, measured in parallel (●) and perpendicular (▲) directions to the columnar axis, as well as in random alignment (■). The dash line indicates the Col<sub>h</sub>-Iso phase transition point on heating. (c–e) polarized optical microscope images of BPO/LiTB(3.5) in the Col<sub>h</sub> LC phase at room temperature: (c) Random alignment of polydomain columns, (d) uniaxial planar oriented columns aligned parallel to the electric field, and (e) Columns oriented perpendicular to the electric field. Arrows denote the direction of the analyser (A), polariser (P), and shearing (S).

### 3.3. Ionic conductivities

AC impedance spectroscopy was used to measure the ionic conductivity of the electrolyte. Figure 3(a) illustrates the ionic conductivities of BPO/LiTB(*x*) at 25°C as a function of the LiTB ratio. It was observed that as the molar ratio of lithium ions increased, the ionic conductivity increased linearly. Specifically, the ionic conductivity of BPO/LiTB(3.5) reached a maximum of  $2.3 \times 10^{-4}$  S cm<sup>-1</sup>. This trend contrasts with that observed in cyclic carbonate-based liquid crystals, where ionic conductivity typically decreases with increasing lithium salt concentration [13]. This observation, along with our previous research, indicates that phosphates exhibit superior lithium-ion transport properties in LC systems.

To confirm the presence of 3D continuous ion pathways in BPO/LiTB(*x*), we aligned the self-assembled columns of BPO/LiTB(3.5) by shearing the material between comb-shaped gold electrodes. This setup allowed for measuring conductivities parallel ( $\sigma_{||}$ ) and perpendicular ( $\sigma_{\perp}$ ) to the columnar axis (Figure 3(b–e) and Fig. S4). The ionic conductivity of BPO/LiTB(3.5) with polydomain

alignment ( $\sigma$ ) was also assessed to compare ion transport capabilities under different orientations as temperature varied. During the heating process, it was observed that prior to the Col<sub>h</sub>-Iso phase transition, the ionic conductivity followed the order  $\sigma_{||} > \sigma > \sigma_{\perp}$ . Notably, the values across the three orientations were relatively close, with a  $\sigma_{||}$  to  $\sigma_{\perp}$  ratio of only 1.2, contrasting with many columnar liquid crystals featuring 1D ion transporting channels, where this ratio often exceeds 10<sup>2</sup> [33–35]. This consistent ionic conductivity observed across all orientations in BPO/LiTB(3.5) suggests the presence of columnar 3D pathways. Additionally, the values of  $\sigma_{||}$  and  $\sigma$  in the Col<sub>h</sub> phase exceeded those estimated by extrapolating the temperature dependence of conductivity in the isotropic liquid phase. The temperature-dependent growth rates of  $\sigma_{||}$  and  $\sigma$  decreased at the Col<sub>h</sub>-Iso phase transition, likely due to the disruption of the self-assembled columnar phase. These findings underscore the critical role of the self-assembled 3D ion pathways in facilitating efficient ion transport.



### 3.4. Actuation performances

In this study, we infused a columnar LC electrolyte into a commercially available microporous polyethylene membrane (HIPORE<sup>TM</sup>) to create a novel free-standing polymer composite electrolyte, significantly simplifying the preparation of iEAP actuators. To verify the porous structure of the polyethylene membrane, we obtained an FE-SEM image, revealing that the majority of the pore sizes are approximately 100 nm (Fig. S5). XRD analysis of the composite electrolyte confirmed that BPO/LiTB(3.5) retains its columnar LC phase. The peak positions of the composite electrolyte membrane exhibited minimal differences compared to the pure LC electrolyte, indicating that the microporous polyethylene membrane has a negligible impact on the LC phase (Fig. S6). This liquid crystal-filled electrolyte membrane was sandwiched between free-standing conductive polymer films made of PEDOT:PSS to construct an actuator.

The columnar LC electrolyte exhibited sufficient mechanical strength, demonstrating self-standing properties and eliminating concerns of fluid leakage from the membrane during actuation. Figure 4(a) shows photographs of the actuator under a 2 V AC voltage. Notably, the actuator exhibits greater bending displacement at  $\pm 2$  V and 0.01 Hz compared to  $\pm 2$  V at 0.1 Hz. When a +2 V voltage is applied to the upper side, the actuator bend towards the anode, indicating that, despite their smaller volume relative to anions, lithium ion determine the bending direction in PEDOT:PSS-based actuators, consistent with previous findings.

We further examined the frequency-dependent bending displacement at different AC square wave voltages (Figure 4(b)). The peak-to-peak displacement under  $\pm 2$  V is more than double that under  $\pm 1$  V across nearly all frequencies, as higher voltages enhance ion dissociation and mobilize ions to the opposite electrode, assisted by phosphate polarity. The actuator achieves peak-to-peak strains of 0.52

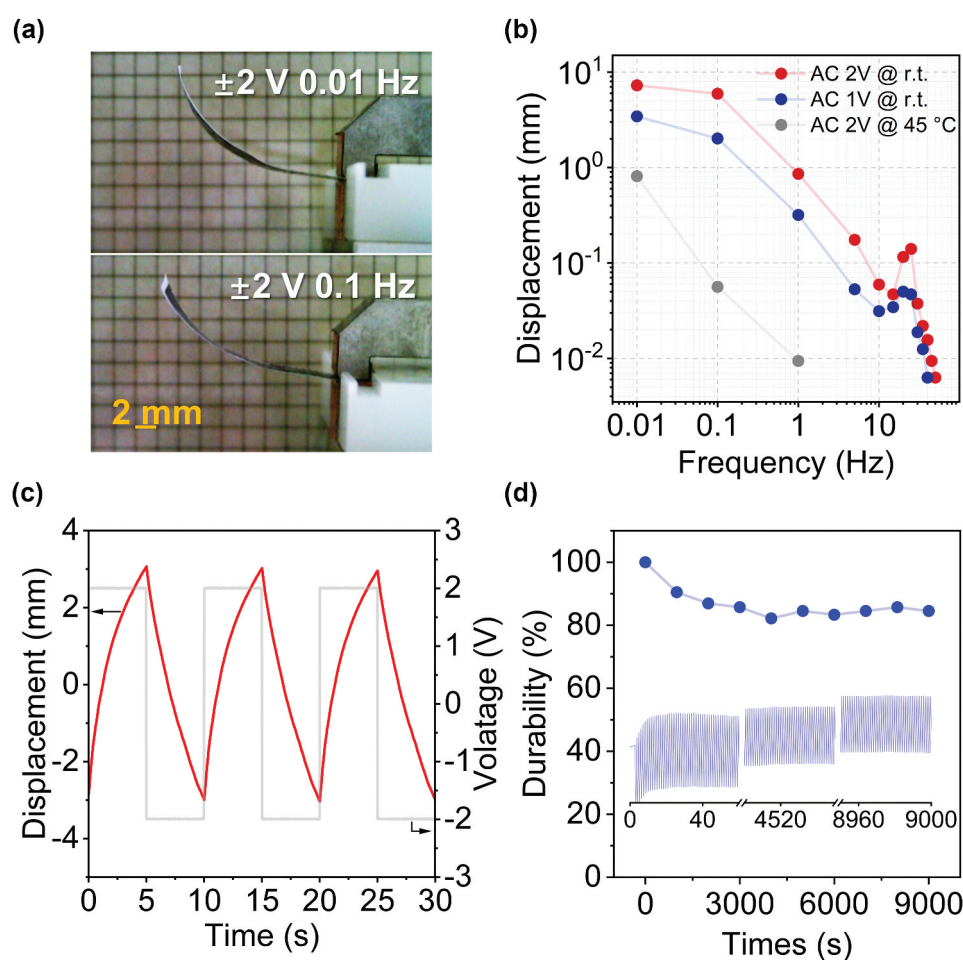


**Figure 4.** (a) Photographs of the bending actuators, composed of a polyethylene-based porous membrane infiltrated with the columnar LC BPO/LiTB(3.5), sandwiched between two PEDOT:PSS electrodes and clamped between stainless steel contacts. The images show the actuators at its maximum bending displacement under  $\pm 2$  V at frequencies of 0.01 and 0.1 Hz. (b) Peak-to-peak displacement of the BPO/LiTB(3.5)-based actuator as a function of frequency. (c) Bending response curve of the BPO/LiTB(3.5)-based actuator under an applied voltage of  $\pm 2$  V at 0.1 Hz. (d) Bending durability of the BPO/LiTB(3.5)-based actuator over repeated cycles.



and 0.46% at  $\pm 2$  V for 0.01 and 0.1 Hz, respectively, while corresponding values at  $\pm 1$  V are 0.31 and 0.19%. At its maximum operating frequency of 50 Hz under  $\pm 2$  V, the actuator reaches a peak-to-peak displacement of  $6.3\ \mu\text{m}$  at 12 mm from the clamped end. Given that human skin sensory cells can perceive vibrations as low as around  $2\ \mu\text{m}$  at high frequencies, this performance positions the actuator as a promising material for tactile applications. To investigate the effect of temperature on the actuator, we placed the actuator in an environment at  $45^\circ\text{C}$ , where the electrolyte transitioned from the  $\text{Col}_h$  phase to the Iso phase. A significant decline in performance was observed, with the peak-to-peak displacement decreasing from 7.27 mm to 0.81 mm under an applied  $\pm 2$  V at 0.01 Hz (Figure 4(b) and Fig. S7). Additionally, the actuator generates a force output of 0.5 mN under  $\pm 2$  V at 0.1 Hz, exceeding the 0.35 mN force produced by layered phosphate – polymer composite actuators in previous studies (Fig. S8). Figure 4(c) further demonstrates the actuator's bending direction aligns with the applied voltage, suggesting lithium ions as the primary driver of the bending response.

CV measurements were performed within a voltage range of  $\pm 1$  V, with scan rates from 10 to  $100\ \text{mV s}^{-1}$  (Fig. S9). As the scan rate decreases, current density also declined, resulting in increased capacitance and a more rectangular  $V$ – $I$  profile. Specific capacitances were measured at 16.0, 10.7, and  $6.73\ \text{mF cm}^{-2}$  at scan rates of 10, 50, and  $100\ \text{mV s}^{-1}$ , respectively. The reduced specific capacitance at high scan rates occurs because ions cannot move quickly enough to the opposite electrode, aligning with the observed decrease in bending displacement at higher frequencies. Additionally, neither low nor high scan rate  $V$ – $I$  profiles exhibited significant redox peaks. Although  $\text{PEDOT}^+$  undergoes continuous oxidation-reduction during charging and discharging, the high conductivity of the electrolyte enables rapid processes that may not clearly appear in the  $V$ – $I$  profiles.

Long-term cycling durability was evaluated as an essential performance metric for the actuator. Figure 4d reveals some initial decline in bending displacement at  $\pm 2$  V, 1 Hz within the first 4000 cycles. However, after this point, displacement stabilizes and even shows slight improvement, likely due to deeper electrolyte infiltration into the electrodes during the bending process, which enhances electrode utilization.

The bending strain and maximum response frequency of BPO/LiTB(3.5)/polyethylene-based actuators were compared with those of various actuators employing PEDOT:PSS electrodes reported in the literature (Fig. S10). Relative to actuators based on ionic LC polymers with 1D and 3D channels [22,36], 3D

liquid crystal/polyvinyl alcohol (PVA) composites [28], ionic liquid/Nafion composites [37–41], polyurethane ion gels [42–44], and ionic covalent organic frameworks [45], our actuator exhibits highly competitive performance. Although its performance does not surpass that of actuators fabricated using vinyl polymers – phosphate-based layered liquid crystal composite electrolytes from our previous studies [23], the columnar phosphate LC electrolyte embedded in a porous polymer membrane in this work offers significant fabrication advantages. It enables precise control over the liquid crystal content and membrane size, making it a cost-effective and practical solution for real-world applications.

## 4. Conclusions

This study presents a new class of 3D lithium-ion-conducting hexagonal columnar liquid crystals, created from tapered phosphate molecules complexed with lithium salts. These liquid crystals demonstrate ionic conductivities of up to  $2 \times 10^{-4}\ \text{S cm}^{-1}$  at room temperature. Integrating this LC electrolyte into a scalable polyolefin-based porous membrane offers exciting potential for actuator applications in soft robotics and wearable electronics. This work not only advances materials innovation but also establishes a versatile platform for next-generation electromechanical devices, where durable, high-performance, and flexible actuation is critical.

## Disclosure statement

No potential conflict of interest was reported by the author(s).

## Funding

This work was supported by JST, PRESTO [Grant Number JPMJPR23QB], JSPS KAKENHI [Grant Number 21H02021], Iketani Science and Technology Foundation [Grant Number 0351202-A], and Murata Science and Education Foundation [Grant Number HTF0202].

## ORCID

Masafumi Yoshio  <http://orcid.org/0000-0002-1442-4352>

## References

- [1] Percec V, Johansson G, Heck J, et al. Molecular recognition directed self-assembly of supramolecular cylindrical channel-like architectures from 6,7,9,10,12,13,15,16-octahydro-1,4,7,10,13-pentaoxabenzocyclopentadecen-2-ylmethyl 3,4,5-Tris(p-dodecyloxybenzyl-oxy) benzoate. *J Chem Soc Perkin Trans.* 1993;1(13):1411–1420. doi: 10.1039/p19930001411
- [2] Beginn U, Zipp G, Mourran A, et al. Membranes containing oriented supramolecular transport

- channels. *Adv Mater.* **2000**;12:513–516. doi: [https://doi.org/10.1002/\(SICI\)1521-4095\(200004\)12:7%3C513::AID-ADMA513%3E3.0.CO;2-S](https://doi.org/10.1002/(SICI)1521-4095(200004)12:7%3C513::AID-ADMA513%3E3.0.CO;2-S)
- [3] Ramón-Gimenez L, Storz R, Haberl J, et al. Anisotropic ionic mobility of lithium salts in lamellar liquid crystalline polymer networks. *Macromol Rapid Commun.* **2012**;33(5):386–391. doi: [10.1002/marc.201100792](https://doi.org/10.1002/marc.201100792)
  - [4] Kerr RL, Miller SA, Shoemaker RK, et al. New type of Li Ion Conductor with 3D interconnected nanopores via polymerization of a liquid organic electrolyte-filled lyotropic liquid-crystal assembly. *J Am Chem Soc.* **2009**;131(44):15972–15973. doi: [10.1021/ja905208f](https://doi.org/10.1021/ja905208f)
  - [5] Kato T, Yoshio M, Ichikawa T, et al. Transport of ions and electrons in nanostructured liquid crystals. *Nat Rev Mater.* **2017**;2(4):17001. doi: [10.1038/natrevmats.2017.1](https://doi.org/10.1038/natrevmats.2017.1)
  - [6] Cho B-K. Nanostructured organic electrolytes. *RSC Adv.* **2014**;4(1):395–405. doi: [10.1039/C3RA45044A](https://doi.org/10.1039/C3RA45044A)
  - [7] Ichikawa T, Kato T, Ohno H. Dimension control of ionic liquids. *Chem Commun.* **2019**;55(57):8205–8214. doi: [10.1039/C9CC04280F](https://doi.org/10.1039/C9CC04280F)
  - [8] Onuma T, Hosono E, Takenouchi M, et al. Noncovalent approach to Liquid-Crystalline Ion Conductors: high-rate performances and room-temperature operation for Li-Ion batteries. *ACS Omega.* **2018**;3(1):159–166. doi: [10.1021/acsomega.7b01503](https://doi.org/10.1021/acsomega.7b01503)
  - [9] Högberg D, Soberats B, Yatagai R, et al. Liquid-crystalline dye-sensitized solar cells: design of two-dimensional molecular assemblies for efficient ion transport and thermal stability. *Chem Mater.* **2016**;28(18):6493–6500. doi: [10.1021/acs.chemmater.6b01590](https://doi.org/10.1021/acs.chemmater.6b01590)
  - [10] Luo J, You J, Tan S, et al. Lamellar lyotropic liquid crystal superior to micellar solution for proton conduction in an aqueous solution of 1-tetradecyl-3-methylimidazolium hydrogen sulfate. *ACS Appl Mater Interface.* **2020**;12(40):45611–45617. doi: [10.1021/acsami.0c13349](https://doi.org/10.1021/acsami.0c13349)
  - [11] Ichikawa T, Yamada T, Aoki N, et al. Surface proton hopping conduction mechanism dominant polymer electrolytes created by self-assembly of bicontinuous cubic liquid crystals. *chem Sci.* **2024**;15(19):7034–7040. doi: [10.1039/D4SC01211A](https://doi.org/10.1039/D4SC01211A)
  - [12] Yazaki S, Funahashi M, Kato T. An electrochromic nanostructured liquid crystal consisting of  $\pi$ -conjugated and ionic moieties. *J Am Chem Soc.* **2008**;130(40):13206–13207. doi: [10.1021/ja805339q](https://doi.org/10.1021/ja805339q)
  - [13] Sakuda J, Hosono E, Yoshio M, et al. Liquid-crystalline electrolytes for lithium-ion batteries: ordered assemblies of a mesogen-containing carbonate and a lithium salt *adv. Funct Mater.* **2015**;25(8):1206–1212. doi: [10.1002/adfm.201402509](https://doi.org/10.1002/adfm.201402509)
  - [14] Ward IM, McIntyre JE, Davies GR, et al. Ionic conduction in sequentially ordered thermotropic liquid-crystalline polymers. *Electrochim Acta.* **1992**;37(9):1479–1481. doi: [10.1016/0013-4686\(92\)80093-2](https://doi.org/10.1016/0013-4686(92)80093-2)
  - [15] Ungar G, Batty SV, Percec V, et al. Structure and conductivity of liquid crystal channel-like linic complexes of taper-shaped compounds. *Adv Mater For Optics Elec.* **1994**;4(4):303–313. doi: [10.1002/amo.860040410](https://doi.org/10.1002/amo.860040410)
  - [16] Iinuma Y, Kishimoto K, Sagara Y, et al. Uniaxially parallel alignment of a smectic a liquid-crystalline Rod-Coil molecule and its lithium salt complexes using rubbed polyimides. *Macromolecules.* **2007**;40(14):4874–4878. doi: [10.1021/ma070160w](https://doi.org/10.1021/ma070160w)
  - [17] Cao S, Yoshio M, Seki A. Ion-conductive nanostructured polymer films formed by photopolymerization of lyotropic columnar liquid-crystalline monomers, composed of a zwitterionic compound and a protic ionic liquid. *Crystals.* **2020**;10(4):276. doi: [10.3390/cryst10040276](https://doi.org/10.3390/cryst10040276)
  - [18] Nguyen VH, Kim J, Tabassian R, et al. Electroactive artificial muscles based on functionally antagonistic core-shell polymer electrolyte derived from PS- *b* - PSS block copolymer. *Sci.* **2019**;6(5):1801196. doi: [10.1002/advs.201801196](https://doi.org/10.1002/advs.201801196)
  - [19] Kim O, Kim H, Choi UH, et al. One-volt-driven superfast polymer actuators based on single-ion conductors. *Nat Commun.* **2016**;7(1):13576. doi: [10.1038/ncomms13576](https://doi.org/10.1038/ncomms13576)
  - [20] Kim O, Shin TJ, Park MJ. Fast low-voltage electroactive actuators using nanostructured polymer electrolytes. *Nat Commun.* **2013**;4(1):2208. doi: [10.1038/ncomms3208](https://doi.org/10.1038/ncomms3208)
  - [21] Nguyen VH, Oh S, Mahato M, et al. Functionally antagonistic polyelectrolyte for electro-ionic soft actuator. *Nat Commun.* **2024**;15(1):435. doi: [10.1038/s41467-024-44719-z](https://doi.org/10.1038/s41467-024-44719-z)
  - [22] Wu C-H, Meng W, Iakoubovskii K, et al. Photocured liquid-crystalline polymer electrolytes with 3D ion transport pathways for electromechanical actuators. *ACS Appl Mater Interface.* **2023**;15(3):4495–4504. doi: [10.1021/acsami.2c19382](https://doi.org/10.1021/acsami.2c19382)
  - [23] Liu C, Cao S, Yoshio M. Ion-conducting non-flammable liquid crystal-polymer composites for high-frequency soft actuators. *Funct Mater.* **2023**;33(25):2300538. doi: [10.1002/adfm.202300538](https://doi.org/10.1002/adfm.202300538)
  - [24] Lee DH, Yang JC, Sim JY, et al. Bending sensor based on controlled microcracking regions for application toward wearable electronics and robotics. *ACS Appl Mater Interface.* **2022**;14(27):31312–31320. doi: [10.1021/acsami.2c07795](https://doi.org/10.1021/acsami.2c07795)
  - [25] Ham H, Park M, Park T, et al. Teleoperation of soft robots with Real-Time fingertip haptic feedback using small batteries. *Adv Mater Technol.* **2023**;8(15):2300070. doi: [10.1002/admt.202300070](https://doi.org/10.1002/admt.202300070)
  - [26] Lascaud S, Perrier M, Vallee A, et al. Phase diagrams and conductivity behavior of Poly(ethylene oxide)-molten salt rubbery electrolytes. *Macromolecules.* **1994**;27(25):7469–7477. doi: [10.1021/ma00103a034](https://doi.org/10.1021/ma00103a034)
  - [27] Cao S, Liu C, Yoshio M. Ionic electroactive PEDOT: PSS/liquid-crystalline polymer electrolyte actuators: photopolymerization of zwitterionic columnar liquid crystals complexed with a protic ionic liquid. *Mater Chem Front.* **2023**;7(14):2828–2838. doi: [10.1039/D3QM00192J](https://doi.org/10.1039/D3QM00192J)
  - [28] Cao S, Aimi J, Yoshio M. Electroactive soft actuators based on columnar ionic liquid Crystal/Polymer composite membrane electrolytes forming 3D continuous ionic channels. *ACS Appl Mater Interface.* **2022**;14(38):43701–43710. doi: [10.1021/acsami.2c11029](https://doi.org/10.1021/acsami.2c11029)
  - [29] Yoneda H, Ikemoto T, Kondo T. Properties of battery separator of polyethylene micro-porous membrane. *Kobunshi Ronbunshu.* **2007**;64(6):394–396. doi: [10.1295/koron.64.394](https://doi.org/10.1295/koron.64.394)
  - [30] Wang J, Yamada Y, Sodeyama K, et al. Fire-extinguishing organic electrolytes for safe batteries. *Nat*

- Energy. 2018;3(1):22–29. doi: [10.1038/s41560-017-0033-8](https://doi.org/10.1038/s41560-017-0033-8)
- [31] Hess A, Barber G, Chen C, et al. Organophosphates as solvents for electrolytes in electrochemical devices *ACS appl. Mater Interface*. 2013;5(24):13029–13034. doi: [10.1021/am403924t](https://doi.org/10.1021/am403924t)
- [32] Zeng G, Xiong S, Qian Y, et al. Non-flammable phosphate electrolyte with high salt-to-solvent ratios for safe potassium-ion battery. *J Electrochem Soc*. 2019;166(6):A1217–22. doi: [10.1149/2.1171906jes](https://doi.org/10.1149/2.1171906jes)
- [33] Yoshio M, Mukai T, Ohno H, et al. One-dimensional ion transport in self-organized columnar ionic liquids. *J Am Chem Soc*. 2004;126(4):994–995. doi: [10.1021/ja0382516](https://doi.org/10.1021/ja0382516)
- [34] Yoshio M, Kagata T, Hoshino K, et al. One-dimensional ion-conductive polymer films: alignment and fixation of ionic channels formed by self-organization of polymerizable columnar liquid crystals. *J Am Chem Soc*. 2006;128(16):5570–5577. doi: [10.1021/ja0606935](https://doi.org/10.1021/ja0606935)
- [35] Choi J-W, Cho B-K. Degree of chain branching-dependent assemblies and conducting behavior in ionic liquid crystalline janus dendrimers. *Soft Matter*. 2011;7(8):4045. doi: [10.1039/c0sm01435d](https://doi.org/10.1039/c0sm01435d)
- [36] Wu C-H, Meng W, Yoshio M. Low-voltage-driven actuators using photo-cross-linked ionic columnar liquid-crystalline polymer films. *ACS Mater Lett*. 2022;4(1):153–158. doi: [10.1021/acsmaterialslett.1c00565](https://doi.org/10.1021/acsmaterialslett.1c00565)
- [37] Kotal M, Kim J, Tabassian R, et al. Highly bendable ionic soft actuator based on nitrogen-enriched 3D hetero-nanostructure electrode. *Adv Funct Mater*. 2018;28(34):1802464. doi: [10.1002/adfm.201802464](https://doi.org/10.1002/adfm.201802464)
- [38] Kim J, Bae S, Kotal M, et al. Soft but powerful artificial muscles based on 3D graphene–CNT–Ni heteronanostructures. *Small*. 2017;13(31):1701314. doi: [10.1002/smll.201701314](https://doi.org/10.1002/smll.201701314)
- [39] Mahato M, Tabassian R, Nguyen VH, et al. Ctf-based soft touch actuator for playing electronic piano. *Nat Commun*. 2020;11(1):5358. doi: [10.1038/s41467-020-19180-3](https://doi.org/10.1038/s41467-020-19180-3)
- [40] Mahato M, Tabassian R, Nguyen VH, et al. Sulfur- and nitrogen-Rich porous  $\pi$ -conjugated COFs as stable electrode materials for electro-ionic soft actuators. *Funct Mater*. 2020;30(46):2003863. doi: [10.1002/adfm.202003863](https://doi.org/10.1002/adfm.202003863)
- [41] Roy S, Kim J, Kotal M, et al. Collectively exhaustive electrodes based on covalent organic framework and antagonistic Co-Doping for electroactive ionic artificial muscles. *Adv Funct Mater*. 2019;29(17):1900161. doi: [10.1002/adfm.201900161](https://doi.org/10.1002/adfm.201900161)
- [42] Wang D, Lu C, Zhao J, et al. High energy conversion efficiency conducting polymer actuators based on PEDOT: PSS/MWCNTs composite electrode. *RSC Adv*. 2017;7(50):31264–31271. doi: [10.1039/C7RA05469F](https://doi.org/10.1039/C7RA05469F)
- [43] Lu F, Xiang K, Wang Y, et al. Electrochemical actuators based on nitrogen-doped carbons derived from zeolitic imidazolate frameworks. *Mater Des*. 2020;187:108405. doi: [10.1016/j.matdes.2019.108405](https://doi.org/10.1016/j.matdes.2019.108405)
- [44] Lu F, Chen T, Xiang K, et al. Ionic electro-active polymer actuator based on cobalt-containing nitrogen-doped carbon/conducting polymer soft electrode. *Polym Test*. 2020;84:106413. doi: [10.1016/j.polymertesting.2020.106413](https://doi.org/10.1016/j.polymertesting.2020.106413)
- [45] Yu F, Ciou J-H, Chen S, et al. Ionic covalent organic framework based electrolyte for fast-response ultra-low voltage electrochemical actuators. *Nat Commun*. 2022;13(1):390. doi: [10.1038/s41467-022-28023-2](https://doi.org/10.1038/s41467-022-28023-2)